The Astrophysical Journal, 662:1245–1253, 2007 June 20

MODERATE-RESOLUTION *SPITZER* INFRARED SPECTROGRAPH OBSERVATIONS OF M, L, AND T DWARFS

A. K. Mainzer,[1] Thomas L. Roellig,[2] D. Saumon,[3] Mark S. Marley,[4] Michael C. Cushing,[5,6] G. C. Sloan,[7] J. Davy Kirkpatrick,[8] S. K. Leggett,[9] and John C. Wilson[10]

Received 2006 September 27; accepted 2007 January 12

ABSTRACT

We present 10–19 μm moderate-resolution spectra of 10 M dwarfs, one L dwarf, and two T dwarf systems obtained with the Infrared Spectrograph (IRS) on board the *Spitzer Space Telescope*. The IRS allows us to examine molecular spectroscopic features/lines at moderate spectral resolution in a heretofore untapped wavelength regime. These $R = \lambda/\Delta\lambda \sim 600$ spectra allow for a more detailed examination of clouds and nonequilibrium chemistry, as well as the molecular features of H_2O, NH_3, and other trace molecular species that are the hallmarks of these objects. A cloud-free model best fits our mid-infrared spectrum of the T1 dwarf ϵ Indi Ba, and we find that the NH_3 feature in ϵ Indi Bb is best explained by a nonequilibrium abundance due to vertical transport in its atmosphere. We examined a set of objects (mostly M dwarfs) in multiple systems to look for evidence of emission features, which might indicate an atmospheric temperature inversion, as well as trace molecular species; however, we found no evidence of either.

Subject headings: infrared: stars — stars: late-type — stars: low-mass, brown dwarfs

Online material: color figures

1. INTRODUCTION

Since the discovery of the first brown dwarf (BD) Gl 229B (Nakajima et al. 1995) and the confirmation of other BD candidates (Becklin & Zuckerman 1988; Basri et al. 1996; Rebolo et al. 1996), extensive efforts have been made to characterize the atmospheric features of these objects both theoretically (Allard et al. 2001; Chabrier & Baraffe 2000; Burrows et al. 2001) and observationally (Basri 2000; Kirkpatrick 2005). Most field BDs have been discovered in wide-field optical and near-infrared surveys such as the Two Micron All Sky Survey (2MASS; Skrutskie et al. 2006), the Deep Near-Infrared Southern Sky Survey (DENIS; Epchtein et al. 1997), and the Sloan Digital Sky Survey (SDSS; York et al. 2000). Until recently, these efforts have centered primarily on optical and near-infrared spectroscopy (Kirkpatrick et al. 1991; Geballe et al. 2002; Leggett et al. 2002; McLean et al. 2003), owing to the extreme difficulty of obtaining mid-infrared data from the ground (Matthews et al. 1996; Creech-Eakman et al. 2004; Sterzik et al. 2005). Recent observations by Cushing et al. (2005) have extended ground-based spectroscopy of BDs out to $\sim$4 μm. The launch of the *Spitzer Space Telescope* (Werner et al. 2004) has allowed an unprecedented look at BD atmospheres using the Infrared Array Camera (IRAC; Fazio et al. 2004) and Infrared Spectrograph (IRS; Houck et al. 2004) instruments. Patten et al. (2006) have used the *Spitzer* IRAC instrument to obtain mid-infrared photometry of M, L, and T dwarfs; Cushing et al. (2006) and Roellig et al. (2004) have performed low-resolution spectroscopy of M, L, and T dwarfs using the IRS.

Although the peak flux of these objects is centered near $\lambda \sim 1$ μm, the mid-infrared offers useful opportunities for understanding fundamental properties of BDs. The fundamental bands of many molecular species common in the atmospheres of BDs, including H_2O, NH_3, and CH_4, typically occur in the mid-infrared, where their opacities are more accurately characterized. Signatures of nonequilibrium chemistry as well as silicate, iron, and corundum cloud structures should be apparent in this wavelength regime (Saumon et al. 2003a, 2003b). In addition, $R = 600$ spectroscopy offers the opportunity to test whether or not trace molecular species such as CO_2, C_2H_2, C_2H_4, C_2H_6, and HCN are detectable in multiple systems, perhaps even in emission, as found in our own solar system's giant planets (Orton et al. 2005; Saumon et al. 2003a; Yelle 2000). Emission lines of low-abundance but high-absorption-cross-section species would indicate a temperature inversion or stratosphere, perhaps arising from absorption of a primary star's UV radiation or even dynamical heating. Moderate resolution mid-infrared spectroscopy can potentially allow detailed tests of these ideas.

The low-resolution ($R \sim 90$) mid-infrared BD spectral sequence of Roellig et al. (2004) and Cushing et al. (2006) can be expanded using the moderate-resolution $R = 600$ capability of the *Spitzer* IRS. In this paper, we present IRS $R = 600$ observations from 10 to 19 μm of M, L, and T dwarfs. Section 2 describes the observations, data reduction, and absolute flux calibration of the spectra, and § 3 presents a preliminary comparison of the spectra to model atmospheres. Conclusions are given in § 4.

2. OBSERVATIONS AND DATA REDUCTION

Our sample for the IRS moderate-resolution observations consists of 13 M, one L, and two T dwarfs observed as part of the

[1] Jet Propulsion Laboratory, Pasadena, CA 91109; amainzer@jpl.nasa.gov.
[2] NASA Ames Research Center, Moffett Field, CA 94035; thomas.l.roellig@nasa.gov.
[3] Los Alamos National Laboratory, Applied Physics Division, Los Alamos, NM 87545; dsaumon@lanl.gov.
[4] NASA Ames Research Center, Moffett Field, CA 94035; mmarley@mail.arc.nasa.gov.
[5] Steward Observatory, University of Arizona, Tucson, AZ 85721; mcushing@as.arizona.edu.
[6] Spitzer Fellow.
[7] Astronomy Department, Cornell University, Ithaca, NY 14853; sloan@isc.astro.cornell.edu.
[8] Infrared Processing and Analysis Center, California Institute of Technology, Pasadena, CA 91125; davy@ipac.caltech.edu.
[9] Gemini Observatory, Hilo, HI 96720; sleggett@gemini.edu.
[10] Astronomy Building, University of Virginia, Charlottesville, VA 22903; jcw6z@virginia.edu.

TABLE 1
Log of the IRS $R = 600$ Observations

Object	Spectral Type[a]		AOR Key	On-Source Exposure Time (s)
	Optical	Infrared		
Gl 229A[b]	M1 V	...	4185856	63
Gl 1	M1.5 V	...	3873792	63
G196-3A[b]	M2.5 V	...	3879168	2886
Gl 674	M2.5 V	...	3874304	63
Gl 687	M3 V	...	3874560	38
Gl 849	M3.5 V	...	3873024	188
GJ 1001A[b]	M3.5 V	...	4190464	1950
Gl 65AB[b]	M5.5 V	...	12246784	25
GJ 1111	M6.5 V	...	3876096	964
VB 10	M8	...	3876864	964
DENIS J0559−1404	L8	...	419558	1950
ϵ Indi Ba/Bb[b]	...	T1/T6 Binary	6313730	1950
2MASS J0559−1404	T5	T4.5	16202496	4148

[a] Optical spectral types of the M dwarfs are from Kirkpatrick et al. (1991, 1995), Henry et al. (2004), and Hawley et al. (1996). The DENIS J0559−1404 optical spectral type is from J. D. Kirkpatrick et al. (2007, in preparation). The ϵ Indi Ba/Bb spectral type is from Burgasser et al. (2006). The 2MASS J0559−1404 spectral types are from Burgasser et al. (2003a, 2003b, 2006).

[b] These objects are parts of multiple systems.

"Dim Suns" IRS Science Team Guaranteed Time Observer (GTO) program[11] (Roellig et al. 2004). These objects were drawn from the larger pool of Dim Suns objects (Cushing et al. 2006). They were selected to be sufficiently bright at $R = 600$. Observations for additional comparable objects could not be used since they failed for various reasons. The IRS is composed of four modules capable of performing low- ($R = \lambda/\Delta\lambda \sim 90$) to moderate-resolution ($R = 600$) spectroscopy from 5.3 to 38 μm. We used the Short-High module that covers from 10 to 19 μm at $R = 600$ in 10 orders. A log of the observations, including the *Spitzer* AOR key, spectroscopic mode, and total on-source integration time, is given in Table 1. Although both optical and infrared spectral types are listed in Table 1, we will hereafter use optical types for the M and L dwarfs (Kirkpatrick et al. 1991, 1999) and infrared types for the T dwarfs (Burgasser et al. 2006), unless otherwise noted. In addition, we hereafter abbreviate the numerical portions of the 2MASS, SDSS, and DENIS target designations as Jhhmm±ddmm, where the suffix is the sexigesimal right ascension (hours and minutes) and declination (degrees and arcminutes) at J2000.0 equinox.

The observations consisted of a series of exposures obtained at two positions along each slit. The raw IRS data were processed with the IRS pipeline (ver. S14) at the *Spitzer* Science Center. No dedicated off-sky observations were taken for any of the objects except 2MASS J0559−1404 and Gl 65AB. For these two objects, separate off-source observations of the sky were taken with integration time equal to that of the on-source observations. One of our observations of ϵ Indi Ba/Bb failed due to a bad peak-up, and we ended up with an observation of blank sky. This failed observation was used as a surrogate sky observation for the remaining objects in Table 1. A more detailed discussion of the zodiacal background subtraction methodology is given below.

Postlaunch, the IRS arrays were discovered to suffer from rogue pixels caused by radiation damage. A rogue pixel is a pixel with abnormally high dark current and/or photon responsivity (a hot pixel) that manifests as pattern noise in an IRS image. The term "rogue" was used originally to distinguish pixels whose responsivity was unpredictable, but now the definition of rogue pixels includes those that are permanently as well as temporarily hot. Approximately 0.2% of all pixels in the Short-High array are rogue pixels, a fraction that is increasing with time as the arrays are irradiated throughout the *Spitzer* mission. The amplitude of the typical rogue pixel is many times larger than the relatively weak signals from the faint BD targets. The *Spitzer* Science Center has provided a set of rogue pixel masks for each IRS campaign; these rogue pixels were identified by having dark count rates greater than 4 σ above the mean dark current over the entire array. These masks were augmented with additional lower level rogue pixels found through a careful visual examination of each object's co-added nods. The rogue pixels were masked using the `irsclean_mask` routine provided by the *Spitzer* Science Center.[12] This routine replaces the rogue pixel with an average over the remaining pixels in the spatial direction. It is important to remove rogue pixels from the data, since their effect is to create a sharp spike in the extracted spectrum, mimicking emission-like features.

The data were reduced using the Spectroscopic Modeling Analysis and Reduction tool (SMART; Higdon et al. 2004) written for the IRS. In the case of 2MASS J0559−1404 and Gl 65AB, where dedicated sky observations had been taken, the sky observations were subtracted from the on-source images. Separate sky observations taken at the same time as the science target are beneficial for two reasons: first, the rogue pixels appear in both image and sky frames at approximately the same value, allowing the excess pixel current to largely subtract away. Second, the contribution of the mid-infrared sky background is considerable compared to the BD flux, especially at longer wavelengths. It is necessary to subtract this background level; measuring it directly adjacent to the object eliminates uncertainties in the absolute value of the sky level. For the remainder of the objects, where no dedicated sky measurement was made, no sky was subtracted at this stage of the processing. All spectra were extracted using the full 6 pixel wide aperture and wavelength-calibrated using SMART. The edges of each spectral order were trimmed using an IDL routine.

[11] Databases of known L and T dwarfs can be found at http://www.dwarfarchives.org and http://www.jach.hawaii.edu/~skl/LTdata.html.

[12] The software package `irsclean_mask` can be found at http://ssc.Spitzer.caltech.edu/archanaly/contributed/irsclean/.

For all objects except 2MASS J0559−1404 and Gl 65AB, the missed pointing on ϵ Indi Ba/Bb was used as a substitute sky observation. A spectrum was extracted from this missed pointing in the same manner as the other targets. Before this zodiacal spectrum could be subtracted from the BD spectra, it had to be scaled to match the zodiacal emission level in the direction of the BD target. Since all of these Short-High observations were taken in conjunction with observations using the Short-Low module, the flux seen in the red and blue peak-up cameras in the Short-Low module provided a convenient way to determine the relative zodiacal emission levels. The ratios of the mean backgrounds in the red and blue peak-up arrays between ϵ Indi Ba/Bb and the target were computed. The missed ϵ Indi Ba/Bb pointing was multiplied by these ratios to approximate the difference in zodiacal background levels between ϵ Indi Ba/Bb and other targets. Following extraction of the target spectrum, this substitute sky spectrum was subtracted from the target. Sky subtraction was performed after extraction since the substitute sky was observed at a significantly different time than each of the science targets, therefore requiring a different rogue pixel mask than each of the BDs. The pitfalls of this technique lie in the fact that the sky observations are not contemporaneous spatially or temporally with the target, and the zodiacal background's spectrum varies substantially over the sky. Future IRS Short-High users have been advised by the *Spitzer* Science Center to collect contemporaneous sky observations to avoid this problem.

Observations of the standard star ξ Dra (K2 III) obtained as part of the normal IRS calibration observations were used to remove the instrument relative spectral response function (RSRF) and flux-calibrate the science targets. The standard-star spectra were extracted in a similar fashion to the science targets. A model spectrum from Cohen et al. (2003) was used to remove the intrinsic stellar spectral energy distribution from the raw standard-star spectra. This technique also serves as a first-order correction to fringes caused by interference within the active layer of the detector array. An RSRF was calculated for each of the two nod positions and was applied to each science target's two nods separately. We attempted to remove the remaining fringe signal from our ξ Dra observations using the IRSFRINGE routine provided as part of the SMART data reduction package. According to the *Spitzer* Science Center IRSFRINGE documentation, the fringe amplitude is typically ∼2%–5%. No further attempt at "defringing" the BD data was made, since in BDs, H_2O bands create a complicated pattern of absorption features that could be confused with actual fringes caused by interference in the IRS. Short-High absolute fluxes were compared with the low-resolution data of Cushing et al. (2006) and match to within 7%–8% or better unless otherwise noted. All Short-High data were scaled to match the absolute fluxes of the low-resolution data, which were calibrated using the IRAC band 4 fluxes of Patten et al. (2006).

3. DISCUSSION

3.1. *M Dwarfs*

In M dwarfs (2400 K $\leq T_{\rm eff} \leq$ 3800 K), C, N, and O are found primarily in CO, N_2, and H_2O. The spectral morphology of M dwarfs is therefore shaped primarily by H_2O absorption bands, although TiO and VO bands dominate in the optical. Since N_2 is a homonuclear molecule, it cannot radiate in the dipole approximation and therefore shows no spectral signatures in M and L dwarfs. The primary feature of interest in the mid-infrared spectra of M dwarfs is the "break" due to the ν_2 fundamental absorption feature of H_2O at ∼6.5 μm. Since the shortest wavelength observable with the IRS Short-High module is 10 μm, this feature is unobservable in our $R = 600$ spectrum. The M dwarf spectra appear featureless in the Short-High data. Figure 1 depicts the Short-High spectra of our M dwarf sample; the signal-to-noise ratio (S/N) is typically ∼100 for these objects. The dominant error for these high-S/N observations is fringing, ∼2%–5% in amplitude.

3.2. *L Dwarf: DENIS J0255−4700*

Figure 2 depicts the sole L dwarf in our sample, the L8 dwarf DENIS J0255−4700 (Martín et al. 1999; Kirkpatrick et al. 2000). In L dwarf spectra, H_2O and CO absorption strengthens. The mid-L dwarfs also show the onset of the ν_3 fundamental band of CH_4 centered at ∼3.3; however, this feature is not observable in the IRS Short-High module. Although the abundance ratio $CO/CH_4 = 1$ for $T \sim 1100$ K and $P = 1$ bar (Lodders & Fegley 2002), the upper atmospheres of mid-L dwarfs can be cooler than 1100 K even if $T_{\rm eff} \sim 1400$ K, resulting in the appearance of CH_4 in the emergent spectrum. While the 10–20 μm spectral region does not contain any strong CH_4 features, CH_4 is an important absorber at shorter wavelengths and affects the spectral energy distribution via flux redistribution.

As spectral type progresses from L to T, a new molecular feature appears, the 10.5 μm Q-branch band of NH_3 at ∼1200 K. NH_3 becomes the nitrogen-bearing gas species that dominates the spectrum between 10 and 14 μm both because it becomes more abundant ($NH_3/N_2 > 1$ for $T < 700$ K at $P = 1$ bar; Lodders & Fegley 2002) and since N_2 has no observable features in the mid-infrared. These NH_3 features mix with H_2O features, which has a complex band structure throughout the 10–19 μm coverage of the IRS Short-High module. Figure 2 shows the comparison of the 10–12 μm region of our $R = 600$ observation of DENIS J0559−1404 to a cloudy model by Marley et al. (2002); the model has been normalized to the data. We observed DENIS J0559−1404 with S/N ∼ 30 at 10 μm and ∼16 at 19 μm. A composite spectrum for this object extending from the optical through the mid-infrared is best matched by an equilibrium model with $T_{\rm eff} = 1400$ K and $\log g = 5.0$ (M. Cushing 2006, private communication), if the model's absolute flux is uncalibrated. The object's parallax has been measured (Costa et al. 2006); when we adjust the model flux for the measured distance, we predict an absolute flux at 10 μm of ∼14 mJy, significantly higher than the observed 9.4 ± 0.5 mJy. This may be due to the lack of reliable age and gravity measurements for this object, as well as inherent uncertainties in the models; binarity and metallicity variations may also play a role. Also, we are unable to establish the presence of NH_3 in this spectrum. Models indicate that at this effective temperature, a S/N >5000 would be required to detect the strongest NH_3 feature at 10.4 μm. Nevertheless, the models match the individual spectral features (due to H_2O opacity) of this object remarkably well once it is normalized.

Cushing et al. (2006) define an NH_3 index versus spectral type; however, since it is defined as the mean flux of a 0.3 μm window around 10.0 μm, it is not possible to precisely compare this index with the $R = 600$ data presented here, since the IRS Short-High module cuts on at 10.0 μm. The Short-High results are in reasonably good agreement with the Short-Low data, although the systematic offset beyond 12 μm may be due to the lack of a nearby and contemporaneous sky measurement for this object, as described in § 2, or problems with the model. As there is no Short-Low data longward of 15 μm, we cannot compare with Short-Low; however, at shorter wavelengths, the Short-Low and Short-High data match reasonably well.

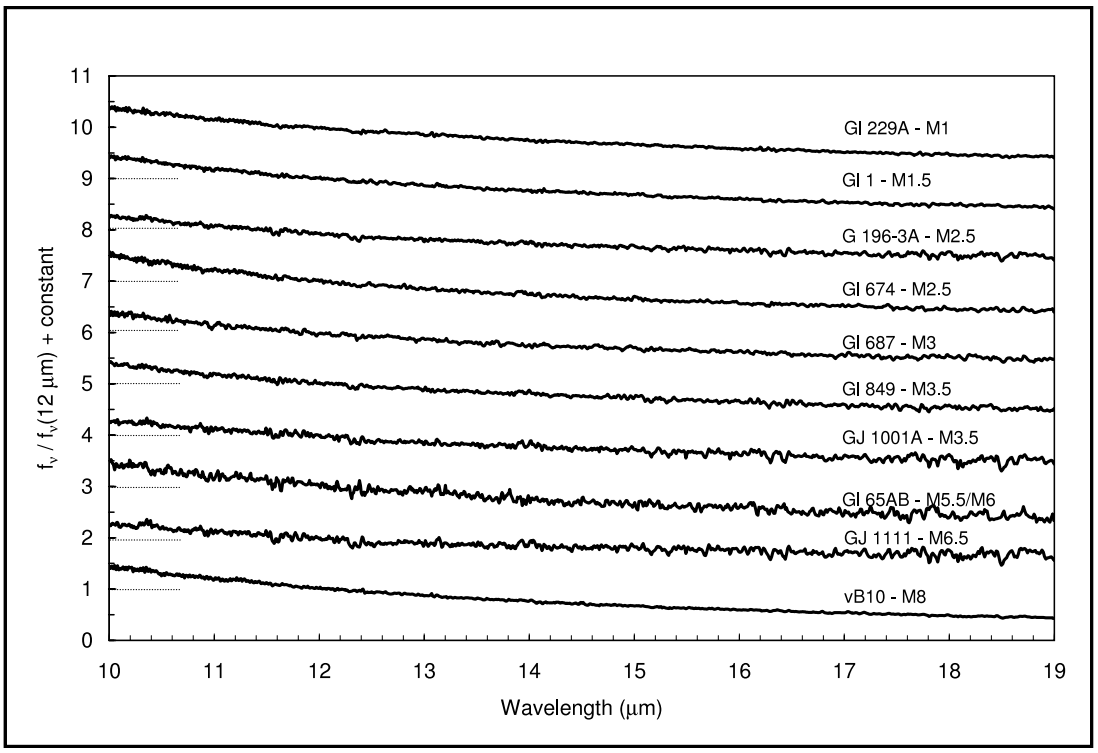

FIG. 1.—Spectral sequence of M dwarfs measured with the IRS Short-High module at $R = 600$. The spectra have been normalized at 12 μm and offset by constants (*dotted lines*); the flux densities at 12 μm are 858 mJy (Gl 229A), 620 mJy (Gl 1), 565 mJy (G196-3A), 429 mJy (Gl 674), 649 mJy (Gl 687), 236 mJy (Gl 849), 452 mJy (GJ 1001A), 365 mJy (Gl 65AB), 842 mJy (GJ 1111), and 538 mJy (VB 10).

3.3. *T Dwarfs: ϵ Indi Ba/Bb and 2MASS J0559−1404*[13]

The CH_4 feature that appears at $T_{\rm eff} \sim 1600$ K becomes very strong in T dwarfs, dominating the spectrum between 7 and 9.2 μm (Cushing et al. 2006; Roellig et al. 2004). The appearance of CH_4 overtone and combination bands in the near-infrared signals the transition to the T spectral class (600 K $\leq T_{\rm eff} \leq$ 1400 K). The Si-, Fe-, and Al-bearing condensates that play a pivotal role in shaping the emergent spectrum of L dwarfs become less critical as they sink below the observable photosphere in T dwarfs, resulting in a largely cloud-free atmosphere in mid to late T dwarfs. The 10.5 μm band of NH_3 overlaps with absorption features of H_2O between 9 and 16 μm as the temperature decreases. Beyond 15 μm, almost all features are due to H_2O, with the exception of weak NH_3 bands between 32 and 46 μm for models with $T_{\rm eff} <$ 800 K (Saumon et al. 2003a).

[13] These sources are also referred to as ϵ Indi BC.

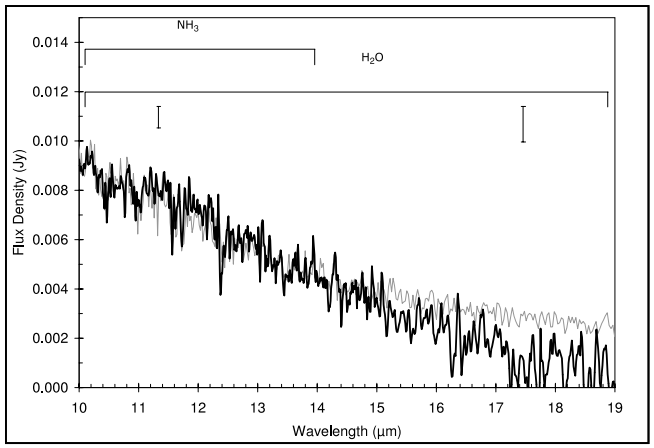

FIG. 2.—Cloudy model (Marley et al. 2002) with $T_{\rm eff} = 1400$ K, $\log g = 4.5$, and sedimentation parameter $f_{\rm sed} = 3$, with NH_3 (*thin line*) compared to the L8 dwarf DENIS J0559−1404 Short-High data (*thick black line*). Typical 1 σ error bars are shown; the uncertainty increases with wavelength. For this object, we did not observe a region of nearby sky. We used the sky from our observation of ϵ Indi Ba/Bb as an approximation; this may be responsible for the mismatch with the model at wavelengths longer than ~15 μm. [*See the electronic edition of the Journal for a color version of this figure.*]

We observed two T dwarfs in our sample, the binary T1/T6 system ϵ Indi Ba/Bb (Scholz et al. 2003), and the T4.5 dwarf 2MASS J0559−1404 (Burgasser et al. 2000).

ϵ Indi Ba/Bb.—The ϵ Indi system consists of three members: a primary K4.5 V star (ϵ Indi A) and a close pair consisting of two T dwarfs separated by 0.732″ (ϵ Indi Ba/Bb; McCaughrean et al. 2004), located 400″ away from the primary. The IRS does not have the spatial resolution to resolve ϵ Indi Ba and Bb, so the measured spectrum is the sum of the two individual spectra. Since in the near-infrared ϵ Indi Ba/Bb is spatially resolved, bright, and very well characterized, and since the metallicity, age, and distance of the primary star (ϵ Indi A) are known, the physical parameters of the Ba and Bb components are very well constrained. The bolometric luminosity of each component (McCaughrean et al. 2004), the age of the system (Lachaume et al. 1999), and the metallicity of ϵ Indi A provide the constraints required to obtain $T_{\rm eff}$ and the gravity from the BD evolution models. The near-infrared data indicate that ϵ Indi Ba has a spectral type of T1 and that ϵ Indi Bb has a spectral type of T6 (McCaughrean et al. 2004). The spectra of late T dwarfs are best modeled with cloudless atmospheres, and we find $T_{\rm eff} = 840$ K and $\log g = 4.89$ for the Bb component using an evolution sequence for cloudless BDs (Roellig et al. 2004). A T1 spectral type falls in the L-T transition where the role of clouds is still unclear, so we consider both cloudy ($f_{\rm sed} = 3$)

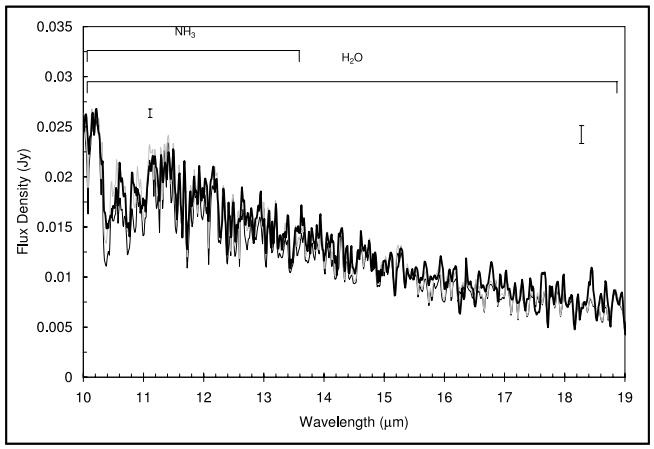

FIG. 3.—Comparison of the observed and modeled mid-infrared spectrum of ϵ Indi Ba/Bb. The data (*thick black line*) are compared to the equilibrium model A (*thin black line*; see Table 2) and the best-fitting model, C (*thin gray line*). The models are plotted at spectral resolution of $R = 600$. The typical 1 σ error is shown; the uncertainty increases with wavelength. [*See the electronic edition of the Journal for a color version of this figure.*]

and cloudless models for the Ba component, giving $T_{\rm eff} = 1210$ K and $\log g = 5.10$ and $T_{\rm eff} = 1250$ K and $\log g = 5.13$, respectively. Typical uncertainties are <90 K on $T_{\rm eff}$ and ~0.15 on $\log g$. With these parameters, the T1 component is about twice as bright in the mid-infrared as the T6 component. The 10–11 μm band of NH_3 is very strong in T6 and essentially absent in T1 dwarfs (Cushing et al. 2006). Nevertheless, the strong NH_3 band in the T6 is easily detected in the combined IRS Short-High spectrum (Fig. 3).

We analyze the NH_3 band in the spectrum of ϵ Indi Ba/Bb by computing composite model spectra for six different cases, considering that the Ba component may or may not be cloudy, and also including the possibility that the NH_3 abundance may be reduced by vertical transport in the atmosphere of both components. Vertical transport in the atmosphere can lead to nonequilibrium abundances for slowly reacting species such as CO and N_2, with the net effect of enhancing the upper atmosphere abundances of CO and N_2 to the detriment of CH_4, H_2O, and NH_3 (Saumon et al. 2003a, 2003b; Fegley & Lodders 1996; Griffith & Yelle 1999; Lodders & Fegley 2002). Evidence for nonequilibrium abundances of NH_3 has been detected in the late T dwarfs Gl 229B and Gl 570D (Saumon et al. 2000, 2003a, 2003b, 2006). The efficiency of vertical transport is parameterized by the vertical eddy diffusion parameter, K_{zz} (Griffith & Yelle 1999). We consider models with $K_{zz} = 0$ (equilibrium), 10^2, and 10^4 cm^2 s^{-1}. The six combinations of parameters are given in Table 2. Cloudy atmospheres are parameterized by a sedimentation parameter, $f_{\rm sed}$ (Ackerman & Marley 2001), which we choose to be $f_{\rm sed} = 3$, a value we found suitable to reproduce the near-infrared colors of early T dwarfs (M. S. Marley et al. 2007, in preparation). Cloudless models have $f_{\rm sed} = \infty$. Given the effective temperature and gravity of each component, the evolution sequences provide their radii. The trigonometric parallax (Perryman et al. 1997) then allows us to compute the absolute composite model flux at Earth to compare with the IRS spectrum, *without any arbitrary renormalization* (Roellig et al. 2004). Figure 3 depicts models A and C from Table 2 compared to our observed $R = 600$ spectrum of ϵ Indi Ba/Bb. The models were smoothed to the IRS Short-High point-source spectral resolution of $\lambda/\Delta\lambda = 600$ using SMART and then binned to the instrument's wavelength sampling.

Figure 4 shows all six models compared to the NH_3 spectral region of ϵ Indi Ba/Bb. Our observation yielded S/N ~50 at 10 μm and ~15 at 19 μm, so the major uncertainty is the overall flux calibration of the Short-Low data to which we scaled the Short-High data. The Short-Low observation of ϵ Indi Ba/Bb has a ±5% flux calibration error (Cushing et al. 2006; Patten et al. 2006). The effects of nonequilibrium chemistry can be seen in the depletion of NH_3 relative to the equilibrium models (A and B). The goodness of fit of the six model spectra is determined by computing the χ^2 between the models and the data. The uncertainty (σ) on the fitted χ^2 is obtained by fitting 5000 simulated data sets generated by adding a random Gaussian noise distribution to each pixel. The Gaussian's width is given by the individual pixel's error bar. The χ^2 fit reveals that the best-fit model is a cloudless nonequilibrium atmosphere with $K_{zz} = 10^2$ cm^2 s^{-1} for both components, model C. Note that both values of K_{zz} used in nonequilibrium models lead to nearly identical mid-infrared spectra as the NH_3 depletion is rather insensitive to the mixing efficiency in late T dwarfs (Saumon et al. 2006). Therefore, model D and model C give equally good fits to the data. Model C is 27 σ better than the best equilibrium model, A. Model C still fits reasonably well (3 σ) even when the data are scaled down by the full 5% flux calibration error. Even though we cannot obtain individual spectra of ϵ Indi Ba and Bb with the IRS, each component's parameters are so well constrained that we find this good evidence of nonequilibrium chemistry in ϵ Indi Bb. The T1 component may be similarly affected, but its higher temperature results in a low NH_3 abundance even in equilibrium, and any nonequilibrium effect would be much less in the hotter component. ϵ Indi Bb joins the ranks of Gl 229B and Gl 570D in a growing set of T dwarfs where nonequilibrium NH_3 abundances have been observed.

TABLE 2
THE SIX MODELS COMPARED TO ϵ INDI Ba/Bb

	Ba					Bb						
MODEL	$T_{\rm eff}$ (K)	$\log g$	$R/R_\odot$	$f_{\rm sed}$	K_{zz} (cm^2 s^{-1})	$T_{\rm eff}$ (K)	$\log g$	$R/R_\odot$	$f_{\rm sed}$	K_{zz} (cm^2 s^{-1})	χ^2	$\Delta\chi^2$
A	1250	5.13	0.0933	NC	0	840	4.89	0.0978	NC	0	26.90	0.35
B	1210	5.10	0.0987	3	0	840	4.89	0.0978	NC	0	21.79	0.30
C	1250	5.13	0.0933	NC	10^2	840	4.89	0.0978	NC	10^2	14.35	0.46
D	1250	5.13	0.0933	NC	10^4	840	4.89	0.0978	NC	10^4	14.11	0.53
E	1210	5.10	0.0987	3	10^2	840	4.89	0.0978	NC	10^2	48.16	0.24
F	1210	5.10	0.0987	3	10^4	840	4.89	0.0978	NC	10^4	63.14	0.24

NOTES.—The six models are compared to ϵ Indi Ba/Bb (Marley et al. 2002), where vertical transport is controlled by varying K_{zz}, the coefficient of vertical eddy diffusion; for cloud sedimentation efficiency ($f_{\rm sed}$; Ackerman & Marley 2001), "NC" indicates cloudless models.

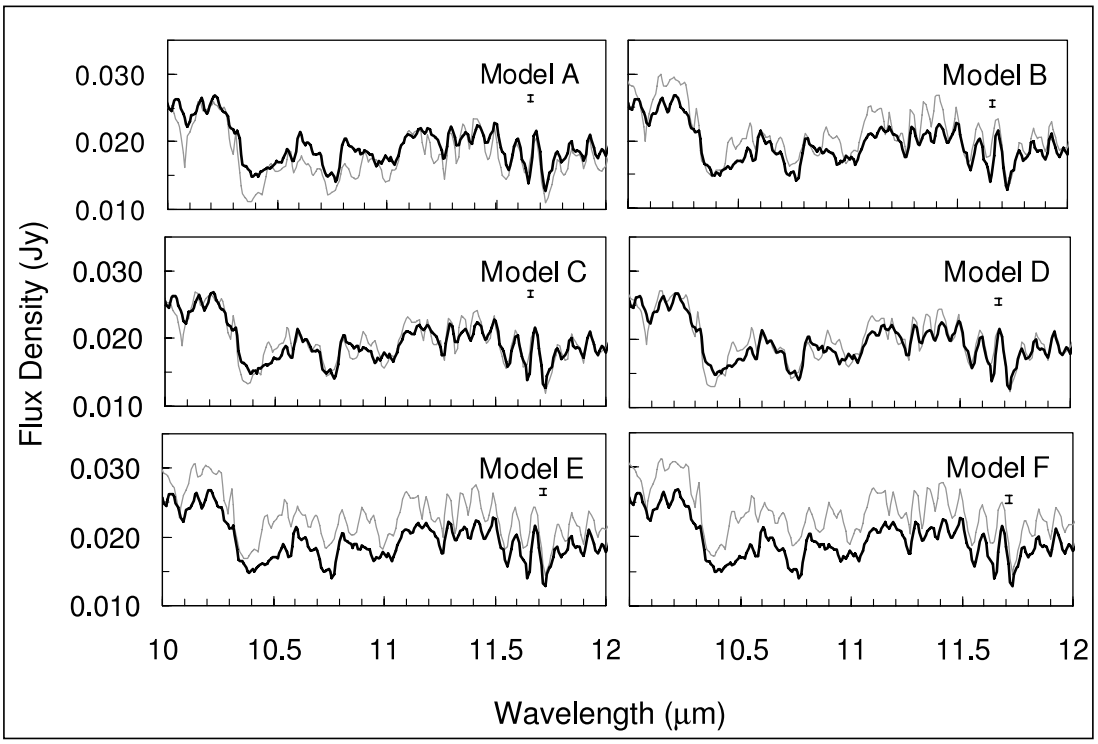

FIG. 4.—Comparison of the 10–12 μm region of the observed $R = 600$ mid-infrared spectrum of ϵ Indi Ba/Bb to the six different models described in Table 2. *Thick black line*: Data. *Thin black line*: Models. The data are best fit by model C, a nonequilibrium cloudless model, which is a significantly better fit than model A, a cloudless equilibrium model. The typical 1 σ error bar is shown.

2MASS J0559−1404.—2MASS J0559−1404 is a T4.5 dwarf (Burgasser et al. 2006). Golimowski et al. (2004) find $T_{\rm eff} \sim 1425$ K if 2MASS J0559−1404 is a single 3 Gyr old dwarf; if it is a multiple system, the $T_{\rm eff}$ will be lower ($\sim$1150 K for an equal-mass pair). It is possible that 2MASS J0559−1404 is actually a multiple system based on its brightness (Burgasser et al. 2000), although efforts to spatially resolve it into multiple components using the *Hubble Space Telescope* have thus far failed (Burgasser et al. 2003a, 2003b). By $T_{\rm eff} \sim 1400$ K, the condensate clouds have sunk to altitudes that are well below the 10 μm photosphere, so they should not directly affect the emergent mid-infrared spectrum of 2MASS J0559−1404. With a T4.5 spectral type, we expect minimal contribution from clouds and the strongest NH_3 band in our sample. The S/N of the Short-High observation ($\sim$14 at 10 μm and 3.5 at 19 μm) is lower than that of ϵ Indi Ba/Bb owing to its greater distance, intrinsic faintness, and slightly higher sky background. Regardless, we clearly observe the NH_3 band in its spectrum (Fig. 5).

The equilibrium model that best fits a composite spectrum extending from optical through mid-infrared wavelengths indicates

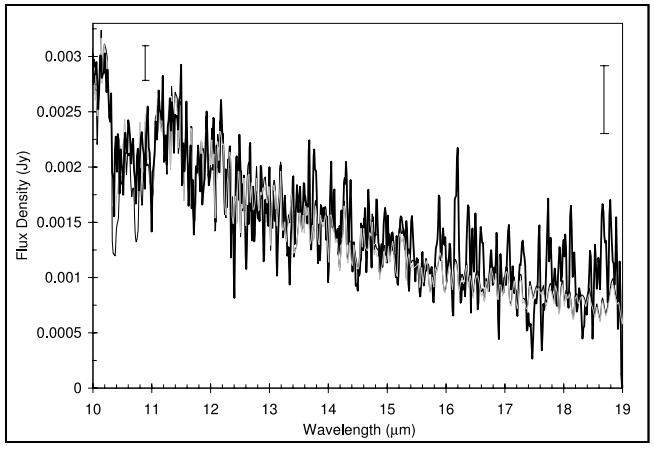

FIG. 5.—Comparison of cloudless models in chemical equilibrium (Marley et al. 2002) with $T_{\rm eff} = 1100$ K, $\log g = 5.477$ (*thin black line*) and $T_{\rm eff} = 1200$ K, $\log g = 5.477$, (*thin gray line*) to the IRS Short-High spectrum of 2MASS J0559−1404 (*thick black line*). Both models have been normalized to the data. Typical 1 σ error bars are shown; the uncertainty increases with wavelength. [*See the electronic edition of the Journal for a color version of this figure.*]

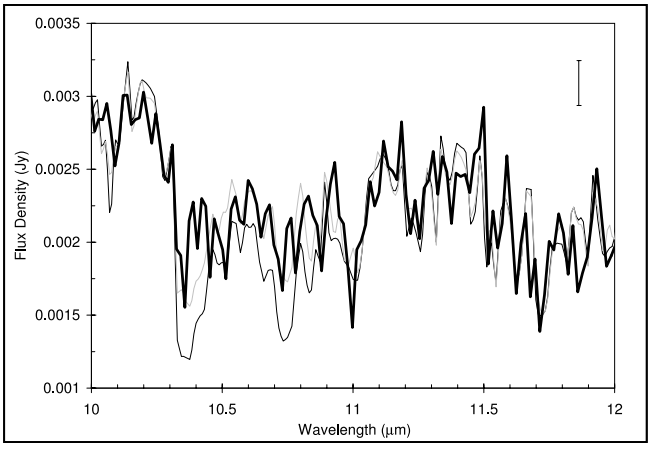

FIG. 6.—Detail of the 10–11 μm NH_3 feature of 2MASS J0559−1404 (*thick black line*) to cloudless models (Marley et al. 2002) with $T_{\rm eff} = 1200$ K, $\log g = 5.0$, $K_{zz} = 0$ cm^2 s^{-1} (equilibrium; *thin black line*) and $K_{zz} = 10^2$ cm^2 s^{-1} (non-equilibrium; *thin gray line*). Both models have been normalized to the data. A typical 1 σ error bar is shown. [*See the electronic edition of the Journal for a color version of this figure.*]

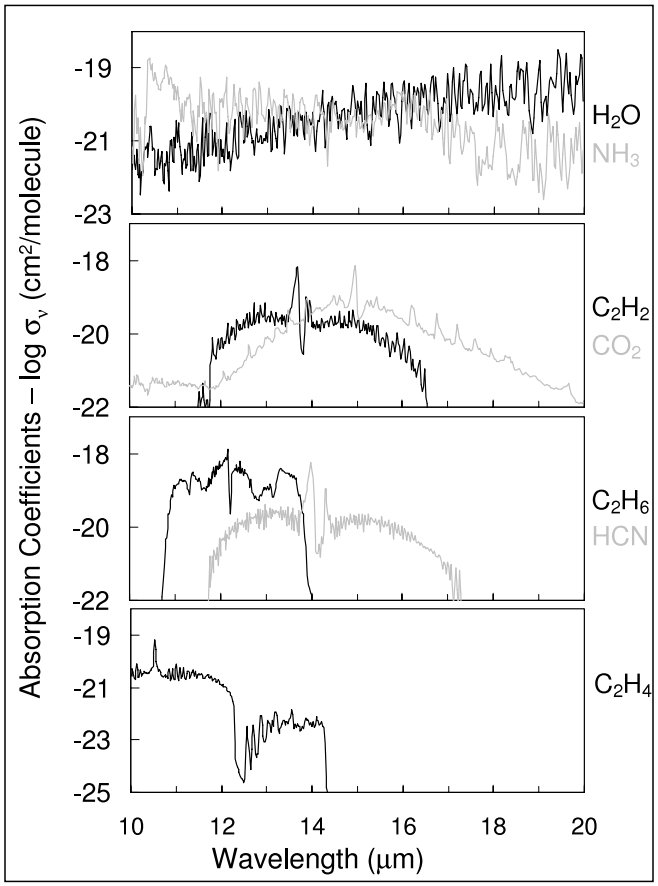

FIG. 7.—Absorption cross section of various molecular species at $R = 600$ that might be expected to occur for $T = 1300$ K and $P = 1$ bar.

that $T_{\rm eff} = 1100$–1200 K and $\log g = 5.0$–5.5, with a cloud sedimentation parameter $f_{\rm sed} = 4$ (M. Cushing 2006, private communication). We find that models with these parameters, assuming that it is a single dwarf and using its known parallax (Dahn et al. 2002), predict a 10 μm flux between 1.3 and 2.3 mJy, compared to the measured 10 μm flux of 2.7 ± 0.2 mJy. Although this may support the notion that this is an unresolved multiple system, this may simply reflect the inherent uncertainties in the models for this object and the lack of a reliable age/gravity. However, we can renormalize the model fluxes to fit only the shape of the spectrum in the region between 10 and 11 μm, which is where differences in the four models are most prominent. We find that of the four equilibrium models studied ($T_{\rm eff} = 1100$ and 1200 K, $\log g = 5.0$ and 5.5), we can only say that the model with $T_{\rm eff} = 1100$ K and $\log g = 5.5$ provides the worst fit at the 6 σ level compared with the other three models, which all had similar χ^2 values within the error bars. When scaled down by the full 5% flux calibration uncertainty, this drops to 3.5 σ.

We attempted to test whether or not nonequilibrium chemistry is apparent in the 10–11 μm NH_3 feature. Fitting the equilibrium and nonequilibrium ($T_{\rm eff} = 1100$, $\log g = 5.0$, $K_{zz} = 10^2$ cm^2 s^{-1}) models to the 10–11 μm region of the Short-High spectrum after normalizing by the flux showed that the nonequilibrium model is preferred at the 2 σ level, but this distinction disappears after scaling down by the full $\pm$5% flux calibration error (Fig. 6). Nonetheless, the models fit the numerous absorption features of NH_3 and H_2O well.

3.4. *Trace Molecular Species*

In L and T dwarf atmospheres, H_2O remains in the gas phase and in the presence of sufficient UV flux can participate in photochemistry, forming such species as HCO and CH_2O (Friedson et al. 2003). For example, solar fluorescence causes both CO and HCN to be observed in emission in the mid-infrared on Neptune, even though it is 30 AU from the Sun, as well as Uranus (Orton et al. 2005; Rosenqvist et al. 1992). In the absence of a stratosphere, these molecules would appear in absorption. The equilibrium abundances of these molecules should be quite low in the absence of photochemistry. Saumon et al. (2003a) calculate the minimum enhancement factor (ϵ) of the abundance of several trace species required for detection. The minimum enhancement factor ϵ is defined as the ratio of the column density of the trace species above the photosphere that is needed for a detection to the chemical equilibrium column density above the photosphere. Table 1 in Saumon et al. (2003a) gives the wavelength of the strongest opacity feature, the $T_{\rm eff}$ that is most favorable for detection, and the enhancement factor. They find that only CO_2 is likely to be detected in absorption, particularly at higher metallicity and lower gravity.

Figure 7 depicts the cross sections of various trace molecular species that might be expected to occur for $\log g = 5$ and $T_{\rm eff} = 1300$ K: CO_2, C_2H_2, C_2H_4, C_2H_6, and HCN (Saumon et al. 2003a). Comparison of these opacities to our data show no signatures of any of these species, although only CO_2 was expected to appear

TABLE 3
MULTIPLE COOL AND ULTRACOOL DWARF SYSTEMS OBSERVED

OBJECT OBSERVED	SPECTRAL TYPE		SEPARATION FROM PRIMARY	
	Primary	Secondary	arcsec	AU
Gl 229AB[a]	M1 V*	T7p	8	48.8
G196-3A[b]	M2.5 V*	L2	16	300
GJ 1001A[c]	M3.5 V*	L4.5+L4.5 (GJ 1001BC)	18	174
G65AB[d,e]	M5.5 V*	M6 V*	2	5.1
VB 10 (Gl 752B)[b]	M2.5 V	M8 V*	3060	521.6
ϵ Indi Ba/Bb[f]	K4.5 V	T1/T6*	400	110

NOTE.—The components that were observed are indicated with an asterisk (*).
[a] Nakajima et al. (1995), Burgasser et al. (2002, 2006).
[b] Kirkpatrick et al. (2001), Rebolo et al. (1998).
[c] Goldman et al. (1999).
[d] Kirkpatrick et al. (1991).
[e] Oppenheimer et al. (2001).
[f] McCaughrean et al. (2004).

at 15 μm in absorption in an equilibrium model with $T_{\rm eff} = 1200$ K and $\log g = 4$. We also considered the effects of LiCl (Weck et al. 2004) and H_2-N_2 (L. Frommhold 2006, private communication); neither of these molecules are expected to have a significant effect on any of the objects we observed compared to NH_3 and H_2O. This indicates that at least at this spectral resolution and sensitivity, trace molecular species have little influence on the emergent spectra of DENIS J0255, 2MASS J0559−1404, and ϵ Indi Ba/Bb.

We observed a number of binary BD systems. In some cases, we observed the system's hotter component, while in others, we observed only the cooler component; in one case, we observed both. In the case of Gl 65AB, we observed both components simultaneously, since with an angular separation of 2″, Gl 65A and Gl 65B are unresolved by the IRS, which has a beam size of ∼2.9″ at 10 μm. The two M dwarfs, an M5.5 and an M6 dwarf (Kirkpatrick et al. 1991), are separated by only 5.1 AU. As shown in Figure 1, no emission lines were detected in our observation of this system, which has the smallest separation between companions in our sample (see Table 3), nor in any of the other binary M dwarfs we surveyed. In another case, we observed a system's secondary: the M8 dwarf VB 10 (Gl 752B), which is separated by ∼522 AU from its companion, the M2.5 dwarf star Gl 752A (Kirkpatrick et al. 1991). Figure 1 shows that its spectrum is also unremarkable. In the case of Gl 229A, we are observing the system's hotter component, and its spectrum reveals no emission features. Fringing effects (as noted above) constitute the dominant error source for these high-S/N observations. Since the fringe signal is ∼2%−5% of the continuum amplitude, a single-bin line would have to have exceed the continuum signal by ∼25% to constitute a 5 σ detection. Our IRS Short-High data do not reveal any unusual spectral features in the mid-infrared spectra of M dwarfs, as is the case at the lower resolution of the IRS Short-Low module (Cushing et al. 2006).

4. CONCLUSIONS

We have presented $R = 600$ spectra of M, L, and T dwarfs from 10 to 19 μm. These spectra have prominent absorption bands of H_2O and NH_3 apparent in the IRS Short-High data. H_2O absorption features are present throughout the M-L-T sequence (although H_2O in M dwarfs is only seen at wavelengths not observable by the IRS Short-High module), while NH_3 appears in T dwarfs. In addition, we find evidence for nonequilibrium chemistry in the atmosphere of the T6 component of the binary ϵ Indi Ba/Bb, providing further support to the concept that vertical transport plays a significant role in T dwarf atmospheres. We found that models with no clouds, at least over the pressure ranges probed by the mid-infrared data, best fit the T1 dwarf ϵ Indi Ba. We find no evidence of emission features, which would have indicated a stratosphere, in any of our targets. We see no evidence of trace molecular species in absorption.

We thank the entire team of the *Spitzer Space Telescope* for their hard work and dedication. This publication makes use of data from the Two Micron All Sky Survey, which is a joint project of the University of Massachusetts and the Infrared Processing and Analysis Center, and funded by the National Aeronautics and Space Administration and the National Science Foundation. This research has made use of the NASA/IPAC Infrared Science Archive, which is operated by the Jet Propulsion Laboratory, California Institute of Technology, under contract with NASA. This research has made use of the SIMBAD database, operated at CDS, Strasbourg, France; NASA's Astrophysics Data System Bibliographic Services; and the M, L, and T dwarf compendium housed at DwarfArchives.org and maintained by Chris Gelino, Davy Kirkpatrick, and Adam Burgasser. This work was supported in part by the United States Department of Energy under contract W-7405-ENG-36. This work is based on observations made with the *Spitzer Space Telescope*, which is operated by the Jet Propulsion Laboratory, California Institute of Technology under NASA contract 1407. Support for this work was provided by NASA's Office of Space Science. A. Mainzer, T. Roellig, and M. Marley would like to acknowledge the support of the NASA Science Mission Directorate.

REFERENCES

Ackerman, A. S., & Marley, M. S. 2001, ApJ, 556, 872
Allard, F., Hauschildt, P. H., Alexander, D. R., Tamanai, A., & Schweitzer, A. 2001, ApJ, 556, 357
Basri, G. 2000, ARA&A, 38, 485
Basri, G., Marcy, G. W., & Graham, J. R. 1996, ApJ, 458, 600
Becklin, E. E., & Zuckerman, B. 1988, Nature, 336, 656
Burgasser, A. J., Geballe, T. R., Leggett, S. K., Kirkpatrick, J. D., & Golimowski, D. A. 2006, ApJ, 637, 1067
Burgasser, A. J., Kirkpatrick, J. D., Liebert, J., & Burrows, A. 2003a, ApJ, 594, 510
Burgasser, A. J., Kirkpatrick, J. D., Reid, I. N., Brown, M. E., Miskey, C. L., & Gizis, J. E. 2003b, ApJ, 586, 512
Burgasser, A. J., et al. 2000, AJ, 120, 1100
———. 2002, ApJ, 564, 421
Burrows, A., Hubbard, W. B., Lunine, J. I., & Liebert, J. 2001, Rev. Mod. Phys., 73, 719
Chabrier, G., & Baraffe, I. 2000, ARA&A, 38, 337
Cohen, M., Wheaton, W. A., & Megeath, S. T. 2003, AJ, 126, 1090
Costa, E., Méndez, R., Jao, W.-C., Henry, T., Subasavage, J., & Ianna, P. 2006, AJ, 132, 1234
Creech-Eakman, M. J., Orton, G. S., Serabyn, E., & Hayward, T. L. 2004, ApJ, 602, L129
Cushing, M. C., Rayner, J. T., & Vacca, W. D. 2005, ApJ, 623, 1115
Cushing, M. C., et al. 2006, ApJ, 648, 614
Dahn, C. C., et al. 2002, AJ, 124, 1170
Epchtein, N., et al. 1997, Messenger, 87, 27
Fazio, G. G., et al. 2004, ApJS, 154, 10
Fegley, B. J., & Lodders, K. 1996, ApJ, 472, L37
Friedson, A. J., Wilson, E., & Moses, J. I. 2003, BAAS, 35, 944
Geballe, T. R., et al. 2002, ApJ, 564, 466
Goldman, B., et al. 1999, A&A, 351, L5
Golimowski, D. A., et al. 2004, AJ, 127, 3516
Griffith, C., & Yelle, R. 1999, ApJ, 519, L85
Hawley, S. L., Gizis, J. E., & Reid, I. N. 1996, AJ, 112, 2799
Henry, T., Subasavage, J., Brown, M., Beaulieu, T., Jao, W.-C., & Hambly, N. 2004, AJ, 128, 2460
Higdon, S. J. U., et al. 2004, PASP, 116, 975
Houck, J. R., et al. 2004, ApJS, 154, 18
Kirkpatrick, J. D. 2005, ARA&A, 43, 195
Kirkpatrick, J. D., Dahn, C. C., Monet, D. G., Reid, I. N., Gizis, J. E., Liebert, J., & Burgasser, A. J. 2001, AJ, 121, 3235
Kirkpatrick, J. D., Henry, T. J., & McCarthy, D. 1991, ApJS, 77, 417
Kirkpatrick, J. D., Henry, T. J., & Simons, D. A. 1995, AJ, 109, 797
Kirkpatrick, J. D., et al. 1999, ApJ, 519, 802
———. 2000, AJ, 120, 447
Lachaume, R., Dominik, C., Lanz, T., & Habing, H. 1999, A&A, 348, 897
Leggett, S. K., et al. 2002, ApJ, 564, 452
Lodders, K., & Fegley, B. 2002, Icarus, 155, 393
Marley, M. S., Seager, S., Saumon, D., Lodders, K., Ackerman, A. S., Freedman, R. S., & Fan, X. 2002, ApJ, 568, 335
Martín, E. L., Delfosse, X., Basri, G., Goldman, B., Forveille, T., & Zapatero Osorio, M. R. 1999, AJ, 118, 2466
Matthews, K., Nakajima, T., Kulkarni, S. R., & Oppenheimer, B. R. 1996, AJ, 112, 1678
McCaughrean, M. J., Close, L. M., Scholz, R.-D., Lenzen, R., Biller, B., Brandner, W., Hartung, M., & Lodieu, N. 2004, A&A, 413, 1029
McLean, I. S., McGovern, M. R., Burgasser, A. J., Kirkpatrick, J. D., Prato, L., & Kim, S. S. 2003, ApJ, 596, 561

Nakajima, T., Oppenheimer, B. R., Kulkarni, S. R., Golimowski, D. A., Matthews, K., & Durrance, S. T. 1995, Nature, 378, 463
Oppenheimer, B. R., Golimowski, D. A., Kulkarni, S. R., Matthews, K., Nakajima, T., & Creech-Eakman, M. 2001, AJ, 121, 2189
Orton, G., Burgdorf, M., Meadows, V., Van Cleve, J., Crisp, D., Stansberry, J., & Atreya, S. 2005, BAAS, 37, 662
Patten, B., et al. 2006, ApJ, 651, 502
Perryman, M. A. C., et al. 1997, A&A, 323, L49
Rebolo, R., Martin, E. L., Basri, G., Marcy, G. W., & Zapatero-Osorio, M. R. 1996, ApJ, 469, L53
Rebolo, R., Zapatero Osorio, M. R., Madruga, S., Bejar, V., Arribas, S., & Licandro, J. 1998, Science, 282, 1309
Roellig, T. L., et al. 2004, ApJS, 154, 418
Rosenqvist, J., Lellouch, E., Romani, P. N., Paubert, G., & Encrenaz, T. 1992, ApJ, 392, L99
Saumon, D., Geballe, T. R., Leggett, S. K., Marley, M. S., Freedman, R. S., Lodders, K., Fegley, B., Jr., & Sengupta, S. K. 2000, ApJ, 541, 374
Saumon, D., Marley, M. S., Cushing, M. C., Leggett, S. K., Roellig, T. L., Lodders, K., & Freedman, R. S. 2006, ApJ, 647, 552
Saumon, D., Marley, M. S., & Lodders, K. 2003a, ApJL, submitted (astro-ph/0310805)
Saumon, D., Marley, M. S., Lodders, K., & Freedman, R. S. 2003b, in IAU Symp. 211, Brown Dwarfs, ed. E. L. Martín (San Francisco: ASP), 345
Scholz, R.-D., McCaughrean, M. J., Lodieu, N., & Kuhlbrodt, B. 2003, A&A, 398, L29
Skrutskie, M. F., et al. 2006, AJ, 131, 1163
Sterzik, M. F., et al. 2005, A&A, 436, L39
Yelle, R. V. 2000, in ASP Conf. Ser. 212, From Giant Planets to Cool Stars, ed. C. A. Griffith & M. S. Marley (San Francisco: ASP), 267
York, D. G., et al. 2000, AJ, 120, 1579
Weck, P. F., Schweitzer, A., Kirby, K., Hauschildt, P. H., & Stancil, P. C. 2004, ApJ, 613, 567
Werner, M. W., et al. 2004, ApJS, 154, 1